Photonic band gap formation in certain self-organizing systems

Kurt Busch and Sajeev John
Department of Physics, University of Toronto, 60 St. George Street, Toronto, Ontario, Canada M5S 1A7
(Received 7 April 1998)

We present a detailed study of photonic band structure in certain self-organizing systems that self-assemble into large-scale photonic crystals with photonic band gaps (PBGs) or pseudogaps in the near-visible frequency regime. These include colloidal suspensions, inverted opals, and macroporous silicon. We show that complete three-dimensional PBGs spanning roughly 10% and 15% of the gap center frequency are attainable by incomplete infiltration of an opal with silicon and germanium, respectively. The photonic band structure of both face center cubic and hexagonal close packed photonic crystals are evaluated. We delineate how the PBG is modified by sintering the opal prior to infiltration and by applying strain along various crystallographic directions. We evaluate the total photon density of states as well as the local density of states (LDOS) projected onto various points within the photonic crystal. It is shown that the LDOS may exhibit considerable pseudogap structure even for systems that do not exhibit a complete PBG. These results are directly relevant to quantum optical experiments in which atoms, dye molecules, or other active materials are inserted into specific locations within the photonic crystal. When the resonant optical transition of these dopants is tuned close to a pseudogap or other abrupt structure in the LDOS, novel effects in radiative dynamics associated with a ''colored vacuum'' may be realized. [S1063-651X(98)11509-X]

PACS number(s): 42.70.Qs, 41.20.Jb, 78.66.Sq

I. INTRODUCTION

Since their proposal in 1987 [1,2], periodic dielectric structures exhibiting a complete photonic band gap (PBG) have generated considerable attention [3–6]. PBG materials facilitate the coherent localization of light [7–9], leading to novel phenomena in quantum optics as well as important technological applications. Although the band structure of classical scalar waves readily yields complete three-dimensional gaps for simple structures such as a face centered cubic lattice of spherical scatterers [10], the vector nature of the electromagnetic wave equation leads to much more restrictive conditions on the dielectric microstructure for the formation of a PBG. Initial difficulties in designing structures that exhibit a complete PBG were allayed by the discovery that the diamond lattice of dielectric spheres exhibits such a frequency range for which (linear) wave propagation is forbidden [11]. In the microwave regime, other diamondlike structures obtained by drilling cylindrical holes in a bulk dielectric material (with a refractive index of 3.5) have been demonstrated to exhibit band gap to center frequency ratios $\Delta\omega/\omega_0$ as large as 20% [12]. Since then, numerous structures amenable to layer by layer fabrication and drilling that possess complete PBG have been suggested [13–16]. A number of structures have already been fabricated with PBGs in the range of millimeter waves [17–19].

These structures not only confirm the soundness of the concept of a PBG but also have interesting applications in the microwave to millimeter wave range. For instance, an antenna mounted on a conventional dielectric constant substrate radiates the majority of its radiation into the substrate itself. If the substrate is engineered into the form of a PBG material with a gap at the radiation frequency, the losses can be minimized, leading to highly directional transmitters [20,21]. Other applications include angular filters [22] and cladding material for preventing losses in waveguide structures that contain bends or junctions [23–25].

Nevertheless, it is for visible and near-infrared frequencies where PBG materials are likely to have their most important impact. For example, applications in telecommunictaions may require the fabrication of large-scale three-dimensional PBG materials with a gap centered around 1.5 μm. These applications may include the design of zero-threshold microlasers, light emitting diodes that exhibit coherence properties at the single photon level, subpicosecond optical switches, and all-optical transistors. In addition, PBG materials represent a frontier in photon-atom interaction phenomena and nonlinear optics. The single greatest obstacle to realizing the potential of PBG materials has been the lack of an inexpensive and reliable means of microfabricating large-scale three-dimensional materials with sizable gaps at near-visible frequencies. In this paper we discuss in detail the possibility of overcoming this obstacle using self-assembling three-dimensional structures based on ''inverted opals.'' Starting from a close-packed face centered cubic lattice of SiO_2 spheres (opal) with diameter on the scale of a micrometer, PBG materials with gaps in the range 5–15 % of the center frequency may be realized by infiltration of the opal with high refractive index materials such as Si or Ge and subsequently removing the SiO_2 by chemical etching. These structures may exhibit a number of novel effects in quantum and nonlinear optics.

While linear wave propagation is absent in the gap of a PBG material, nonlinear propagation effects in the form of ultrashort solitary wave pulses can still occur. Recent studies indicate that as a result of their large group velocity dispersion near a photonic band edge and complex symmetries, PBG materials exhibit a much richer variety of nonlinear wave propagation phenomena than conventional waveguides or optical fibers [26–28]. In addition, PBG materials exhibit

 © 1998 The American Physical Society

different quantum optical features, related to the drastic alteration of the photon density of states (DOS). A vanishing DOS leads to bound photon-atom states [29,30], suppressed spontaneous emission [1,31,32], and strong localization of photons [2,29,30,33]. Unlike conventional microcavities and other confined optical systems, PBG materials support propagation effects on the scale of the localization length for photons leading to different types of cooperative behavior involving photons and atoms. In a PBG material, photon localization effects render the master equation approach of standard quantum optics problematic since localization implies highly non-Markovian memory effects in radiative dynamics. In addition, it requires a nonstandard treatment that goes beyond the Born approximation [34]. Among the phenomena predicted in this frontier of quantum optics are (i) collective switching of two-level atoms from the ground to the excited state with low intensity applied laser fields leading to all-optical transistor action [35], (ii) anomalous superradiant emission rates and low-threshold band-edge lasers [33], (iii) low-threshold nonlinear optical response [36], and (iv) highly nonclassical states of light within the PBG in the form of multiphoton localization and propagating quantum gap solitons [37].

These very exciting prospects for PBG materials with band gaps in the visible region, have triggered numerous efforts to manufacture such structures, with periodicity on the optical scale. Two-dimensional PBG materials [38–41] have reached band gaps (complete in two dimensions and incomplete in three dimensions) around wavelengths of 5 μm and the (electrochemical etching) technique is clearly capable of further downscaling of the structures [42]. In three dimensions a number of self-assembling photonic crystals already exist. These include colloidal systems [43–45] and artificial opals [46–48]. Unfortunately, these readily available photonic crystals do not satisfy the necessary criteria of high index contrast and correct network topology to produce a complete PBG. Theoretical studies, however, indicate the possibility of complete PBG in closely related structures. Binary colloidal mixtures [49] consisting of two sizes of TiO_2 spheres as well as fcc lattices consisting of low dielectric inclusions in a connected high dielectric network (henceforth called inverted structures) exhibit sizable PBGs. The latter possibility has spurred highly interesting work on emulsion templating [50] and on the infiltration of opals with silicon or germanium [51]. We expect that these techniques will soon lead to a large-scale PBG material with a complete three-dimensional gap at near-visible frequencies.

In this paper we investigate in detail the above-mentioned structures from the viewpoint of optimizing the gap size through the manufacturing process. We present results on the total as well as the projected (local) DOS of various structures and discuss their implications on the feasibility of quantum optical experiments in PBG materials. The paper is organized as follows. In Sec. II we will introduce the theoretical and computational framework in which our band structure calculations are performed. Section III contains our results on structures that do not posses a complete PBG, such as colloidal crystals and two-dimensional PBG materials. Section IV is devoted to the study of inverted fcc and hcp structures that exhibit a complete three-dimensional PBG. Finally, in Sec. V we summarize and discuss our findings.

II. THEORETICAL FRAMEWORK

While there are a number of techniques for band structure calculations of electronic crystals, band structures of PBG materials have almost exclusively been obtained from the plane wave expansion method (PWEM). Contrary to the situation for electronic crystals, the ''periodic potentials'' in PBG materials are known from the outset and do not have to be computed in a self-consistent fashion. In this paper we use the PWEM for computing the band structure of two- and three-dimensional PBG materials, the total DOS, as well as the projected (local) DOS.

A. Band structure computation

The PWEM is based on the Bloch-Floquet theorem, which states that eigensolutions of differential equations with periodic coefficients may be expressed as a product of plane waves and lattice-periodic functions. Consequently, all periodic functions are expanded into appropriate Fourier series. Inserting these expansions into the differential equation results in an infinite matrix-eigenvalue problem, which, suitably truncated, provides the eigenfrequencies and expansion coefficients for the eigenfunctions.

We begin by computing the dispersion relations for two-dimensional PBG materials. They consist of periodic arrangements of infinitely extended and parallel oriented cylinders with radius R_0 embedded in dielectric matrix. Here and throughout the paper we consider the embedding matrix material to possess a real, frequency-independent dielectric constant ϵ_a. Similarly, we assume the scattering cylinders, spheres, etc., to consist of material with a real, frequency-independent dielectric constant ϵ_b. To make the problem two dimensional we assume that light propagates perpendicular to the cylinder axis. The latter defines the z axis. For future reference we note here that the periodic dielectric constant $\epsilon_p(\vec{r})$ may then be written as

$$\frac{1}{\epsilon_p(\vec{r})} = \frac{1}{\epsilon_a} + \left(\frac{1}{\epsilon_b} - \frac{1}{\epsilon_a}\right) \sum_{\vec{R}} S(\vec{r} - \vec{R}) \tag{1}$$

$$= \sum_{\vec{G}} \eta_{\vec{G}} e^{i\vec{G}\cdot\vec{r}}, \tag{2}$$

where $\vec{R}$ denotes real space lattice vectors and $\vec{G}$ are the corresponding reciprocal lattice vectors. The function $S(\vec{r})$ takes on the value one if $|\vec{r}| \leq R_0$, where R_0 is the cylinder radius, and is zero otherwise. We note here that for two-dimensional problems all vectors are understood to have two components, whereas for three-dimensional problems all vectors will have three components. The Fourier coefficients $\eta_{\vec{G}}$ are given by

$$\eta_{\vec{G}} = \frac{1}{\Omega} \int_{\mathrm{WSC}} d^2 r \, \frac{1}{\epsilon_p(\vec{r})} e^{-i\vec{G}\cdot\vec{r}}. \tag{3}$$

Here we designate the volume of the Wigner-Seitz cell (WSC) by Ω. For light incident perpendicular to the cylinder axis, the two transverse polarizations decouple, leaving us with two scalar problems. If the electric field is polarized

parallel to the cylinder axis (E polarization), the propagation is governed by the scalar wave equation

$$\frac{1}{\epsilon_p(\vec{r})}\left(\frac{\partial^2}{\partial x^2}+\frac{\partial^2}{\partial y^2}\right)E(\vec{r})+\frac{\omega^2}{c^2}E(\vec{r})=0, \tag{4}$$

where $E(\vec{r})$ is the z component of the electric field. Following the Bloch-Floquet theorem, we expand $E(\vec{r})$ as

$$E_{\vec{k}}(\vec{r})=\sum_{\vec{G}} A_{\vec{G}}^{\vec{k}}\, e^{i(\vec{k}+\vec{G})\cdot\vec{r}}, \tag{5}$$

where $\vec{k}$ is a wave vector lying in the first Brillouin zone (BZ) that labels the eigensolutions of Eq. (4) [52]. Inserting this expansion into Eq. (4) and defining the coefficients $B_{\vec{G}}^{\vec{k}} \equiv |\vec{k}+\vec{G}|A_{\vec{G}}^{\vec{k}}$ yields a symmetric eigenvalue problem

$$\sum_{\vec{G}'} |\vec{k}+\vec{G}||\vec{k}+\vec{G}'|\,\eta_{\vec{G}-\vec{G}'}B_{\vec{G}'}^{\vec{k}}=\frac{\omega_{\vec{k}}^2}{c^2}B_{\vec{G}}^{\vec{k}}. \tag{6}$$

The reciprocal lattice sum is then truncated in order to obtain a numerical solution. In our numerical calculations convergence was established by increasing the number of reciprocal lattice vectors used to truncate Eq. (6) until the final result was independent of the truncation. We found that using 720 reciprocal lattice vectors closest to the origin yields a converged band structure for the dielectric contrasts we have considered.

When the electric field is polarized perpendicular to the cylinder axis (H polarization), the corresponding magnetic field has a z component $H(\vec{r})$ only and we may work with the corresponding wave equation

$$\frac{\partial}{\partial x}\left(\frac{1}{\epsilon_p(\vec{r})}\frac{\partial H(\vec{r})}{\partial x}\right)+\frac{\partial}{\partial y}\left(\frac{1}{\epsilon_p(\vec{r})}\frac{\partial H(\vec{r})}{\partial y}\right)+\frac{\omega^2}{c^2}H(\vec{r})=0. \tag{7}$$

Expanding the magnetic field in the form

$$H_{\vec{k}}(\vec{r})=\sum_{\vec{G}} C_{\vec{G}}^{\vec{k}}\, e^{i(\vec{k}+\vec{G})\cdot\vec{r}}, \tag{8}$$

we arrive at corresponding the symmetric matrix-eigenvalue equation

$$\sum_{\vec{G}'} (\vec{k}+\vec{G})\cdot(\vec{k}+\vec{G}')\,\eta_{\vec{G}-\vec{G}'}C_{\vec{G}'}^{\vec{k}}=\frac{\omega_{\vec{k}}^2}{c^2}C_{\vec{G}}^{\vec{k}}. \tag{9}$$

Truncation of the reciprocal lattice sum follows the same recipe as for Eq. (6).

Fully three-dimensional PBG computations proceed in an essentially analogous fashion. The periodic dielectric constant $\epsilon_p(\vec{r})$ defines a three-dimensional lattice and corresponding three-dimensional reciprocal lattice vectors. The Fourier expansion of $1/\epsilon_p(\vec{r})$ is given by Eq. (1), where the Fourier coefficients [cf. Eq. (3)] are now determined by integrating over the three-dimensional WSC. However, in three dimensions, there is no decoupling of the two transverse polarizations. As a consequence, the full vector problem has to be solved. We do this following the approach of Ho, Chan, and Soukoulis [11], which is based on the wave equation for the magnetic field

$$-\vec{\nabla}\times\left(\frac{1}{\epsilon_p(\vec{r})}\vec{\nabla}\times\vec{H}(\vec{r})\right)+\frac{\omega^2}{c^2}\vec{H}(\vec{r})=0, \tag{10}$$

$$\vec{\nabla}\cdot\vec{H}(\vec{r})=0. \tag{11}$$

The divergence-free magnetic field permits an expansion of the form

$$\vec{H}_{\vec{k}}=\sum_{\vec{G}}\sum_{\lambda} h_{\vec{G}}^{\lambda}\hat{e}_{\vec{G}}^{\lambda}\, e^{i(\vec{k}+\vec{G})\cdot\vec{r}}, \tag{12}$$

where $\hat{e}_{\vec{G}}^{\lambda}$ with $\lambda=1,2$ denote two unit vectors such that the set $\{\hat{e}_{\vec{G}}^{\lambda=1},\hat{e}_{\vec{G}}^{\lambda=2},\vec{k}+\vec{G}\}$ forms an orthogonal triad. The matrix-eigenvalue equation corresponding to Eq. (10) then becomes

$$\sum_{\vec{G}'} |\vec{k}+\vec{G}||\vec{k}+\vec{G}'|\,\eta_{\vec{G}-\vec{G}'}\begin{pmatrix} \hat{e}_{\vec{G}}^2\cdot\hat{e}_{\vec{G}'}^2 & -\hat{e}_{\vec{G}}^2\cdot\hat{e}_{\vec{G}'}^1 \\ -\hat{e}_{\vec{G}}^1\cdot\hat{e}_{\vec{G}'}^2 & \hat{e}_{\vec{G}}^1\cdot\hat{e}_{\vec{G}'}^1 \end{pmatrix}\begin{pmatrix} h_{\vec{G}'}^1 \\ h_{\vec{G}'}^2 \end{pmatrix} = \frac{\omega_{\vec{k}}^2}{c^2}\begin{pmatrix} h_{\vec{G}}^1 \\ h_{\vec{G}}^2 \end{pmatrix}. \tag{13}$$

Again, following Ref. [11], instead of computing the Fourier coefficients $\eta_{\vec{G}-\vec{G}'}$ directly from Eq. (3), we compute the matrix $\epsilon_{\vec{G},\vec{G}'}\equiv\epsilon_{\vec{G}-\vec{G}'}$ of Fourier coefficients of $\epsilon_p(\vec{r})$ for the set of reciprocal lattice vectors that define the truncation of Eq. (13). We then take $\eta_{\vec{G}-\vec{G}'}$ to be the $(\vec{G},\vec{G}')$ element of the inverse of the matrix $\epsilon_{\vec{G},\vec{G}'}$. This procedure is known to drastically improve the convergence of eigenvalue computations from Eq. (13) [53,54]. Using this technique, we required less than 1000 reciprocal lattice vectors to obtain converged band structures. In fact, for most cases 720 reciprocal lattice vector produced results that deviated from the converged results by less than 0.5%. Once Eq. (13) has been solved for both eigenvalues and eigenvectors, the electric field corresponding to a given eigenfrequency $\omega_n(\vec{k})$ can be computed from Eq. (12) using Maxwell's equation

$$\vec{E}_{n,\vec{k}}(\vec{r})=-i\frac{c}{\omega_n(\vec{k})\,\epsilon_p(\vec{r})}\vec{\nabla}\times\vec{H}_{n,\vec{k}} =\sum_{\vec{G}} |\vec{k}+\vec{G}|(h_{\vec{G}}^1\hat{e}_{\vec{G}}^{\,2}-h_{\vec{G}}^2\hat{e}_{\vec{G}}^{\,1})\, e^{i(\vec{k}+\vec{G})\cdot\vec{r}}. \tag{14}$$

Here the subscript n labels the bands. Finally, it follows from the orthonormality of eigenvectors of Eq. (13) that the Bloch functions $\vec{H}_{n,\vec{k}}$ and $\vec{E}_{n,\vec{k}}$ obey the orthonormality relations

$$\int d^3r\ \vec{H}_{n,\vec{k}}(\vec{r})\cdot\vec{H}^*_{n',\vec{k}'}(\vec{r})=\delta(\vec{k}-\vec{k}')\,\delta_{nn'}, \tag{15}$$

$$\int d^3r\ \epsilon_p(\vec{r})\vec{E}_{n,\vec{k}}(\vec{r})\cdot\vec{E}^*_{n',\vec{k}'}(\vec{r})=\delta(\vec{k}-\vec{k}')\,\delta_{nn'}. \tag{16}$$

B. Photon density of states

Transmission experiments on PBG materials usually do not probe all the details of the dispersion relation $\omega_n(\vec{k})$ directly, but rather measure the number of states available for a given direction of propagation. Integrating this number of states over all directions describes the average behavior of the structure under consideration yielding the total DOS. Mathematically, the total DOS $N(\omega)$ is defined as

$$N(\omega)=\sum_n \int_{1.\mathrm{BZ}} d^3k\ \delta(\omega-\omega_n(\vec{k})), \tag{17}$$

where BZ stands for the first Brillouin zone. Since the dispersion relation $\omega_n(\vec{k})$ is generally known only numerically [by solving Eq. (13)], the k-space integral in Eq. (17) has to be suitably discretized. For our computation we use the linear tetrahedron method [55] in its correctly symmetry weighted form [56]. Details for the evaluation of the two-dimensional DOS can be found in the Appendix and for three dimensions we refer to Ref. [56].

For application to quantum optical experiments in PBG materials it is, however, necessary to proceed one step further. Consider an excited atom at some specific location within a PBG material. In order for the atom to decay via a single-photon process it needs to emit a photon into a Bloch mode of the PBG material. Consequently, it is the local coupling (overlap matrix element) of the atomic dipole moment to photons in this mode that determines the decay rate of the excited atom [57,58]. Assuming that an allowed electric dipole transition is the dominant decay channel, we may combine (overall) mode availability and coupling to the mode in the so-called projected or local DOS (LDOS) $N(\omega,\vec{r})$ defined as

$$N(\omega,\vec{r})=\sum_n \int_{1.\mathrm{BZ}} d^3k|E_{n,\vec{k}}(\vec{r})|^2\delta(\omega-\omega_n(\vec{k})), \tag{18}$$

where $E_{n,\vec{k}}(\vec{r})$ are the Bloch functions of Eq. (14). The total DOS can be recaptured from the LDOS using Eq. (16):

$$N(\omega)=\int_{\mathrm{WSC}} d^3r\ \epsilon_p(\vec{r})N(\omega,\vec{r}). \tag{19}$$

This provides a convenient way of checking the accuracy of our k-space integration.

In what follows we will describe the total DOS as well as the LDOS of self-organizing PBG materials. The LDOS will play a crucial role in spontaneous emission dynamics from atoms and molecules placed within a PBG material, non-Markovian behavior in the photon-atom interaction, and collective behavior such as lasing and nonlinear switching effects. In particular, we find that the LDOS may be profoundly different from the total DOS, so that a judicious choice of where in the PBG material dopant atoms are placed may be crucial for the success of quantum optical experiments. In addition, we investigate band structures, the total DOS, and the LDOS of materials that are yet to be fabricated. We hope that this will provide some insight for successfully manufacturing PBG materials with complete PBGs in the visible region, as well as serve as a guide for realizing many of the quantum optical experiments, suggested by theory [29–37,57,58].

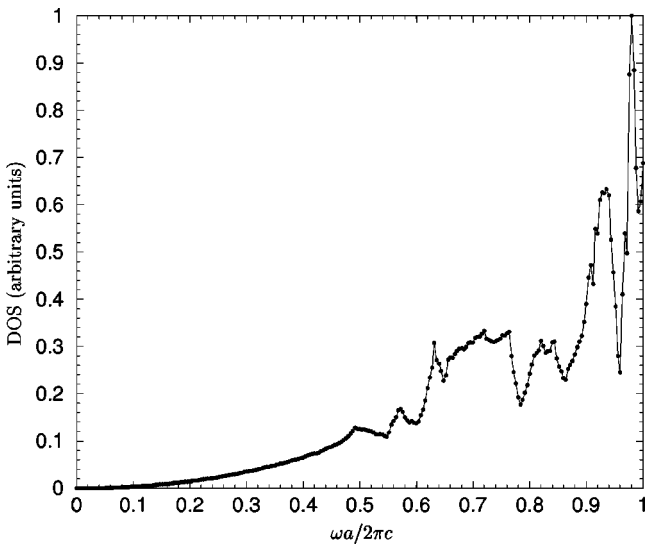

FIG. 1. Total DOS for a fcc lattice of TiO_2 spheres ($\epsilon\approx 7.35$) in water ($\epsilon\approx 1.77$). The filling ratio for TiO_2 is 25%.

III. SYSTEMS WITHOUT A COMPLETE PHOTONIC BAND GAP

As mentioned above, PBG materials that do not possess complete PBGs are readily available and their DOS may nevertheless exhibit rapid variations with frequency, such as pseudo-gaps or Van Hove singularities. Sufficiently large fluctuations in the DOS of these materials may therefore provide a ''colored vacuum'' for several interesting quantum optical experiments. For instance, the relevant input parameters for the fast optical switching and all-optical transistor action of Ref. [35] are (i) the number of atoms, (ii) the applied laser field, and (iii) the ratio γ_+/γ_- of the decay rates between the two closely spaced frequencies $\omega_\pm=\omega_{21}\pm\Delta$ representing the Mollow fluorescence sidebands of a two-level atom. Here ω_{21} is the transition frequency between the excited and the ground state of the bare atom and Δ is the separation of the Mollow side bands of the atom after it is ''dressed'' by an external laser field. In general, a larger ratio $\gamma_+/\gamma_-\propto N(\omega_+,\vec{r})/N(\omega_-,\vec{r})$ will enhance the collective switching effect. However, a ratio as low as $\gamma_+/\gamma_-\approx 2$ will already produce a sizable effect.

A. Colloidal suspension of TiO_2 spheres in water

We first consider a colloidal suspension of TiO_2 spheres with dielectric constant $\epsilon_b\approx 7.35$ in water $\epsilon_a\approx 1.77$. We assume a filling ratio of $f=0.25$ of TiO_2 spheres. Figure 1 shows the total DOS for this particular photonic crystal. Here and in all following graphs we use a dimensionless frequency $\tilde{\omega}=\omega a/2\pi c$, where a is the lattice constant and c denotes the vacuum speed of light. We observe two sharply rising flanks around $\tilde{\omega}\approx 0.62$ [$N(0.600)=0.137$ and $N(0.632)=0.307$] and $\tilde{\omega}\approx 0.90$ [$N(0.864)=0.230$ and $N(0.936)=0.633$]. Consequently, within 5% and 8.5% intervals around the center frequency the total DOS changes by

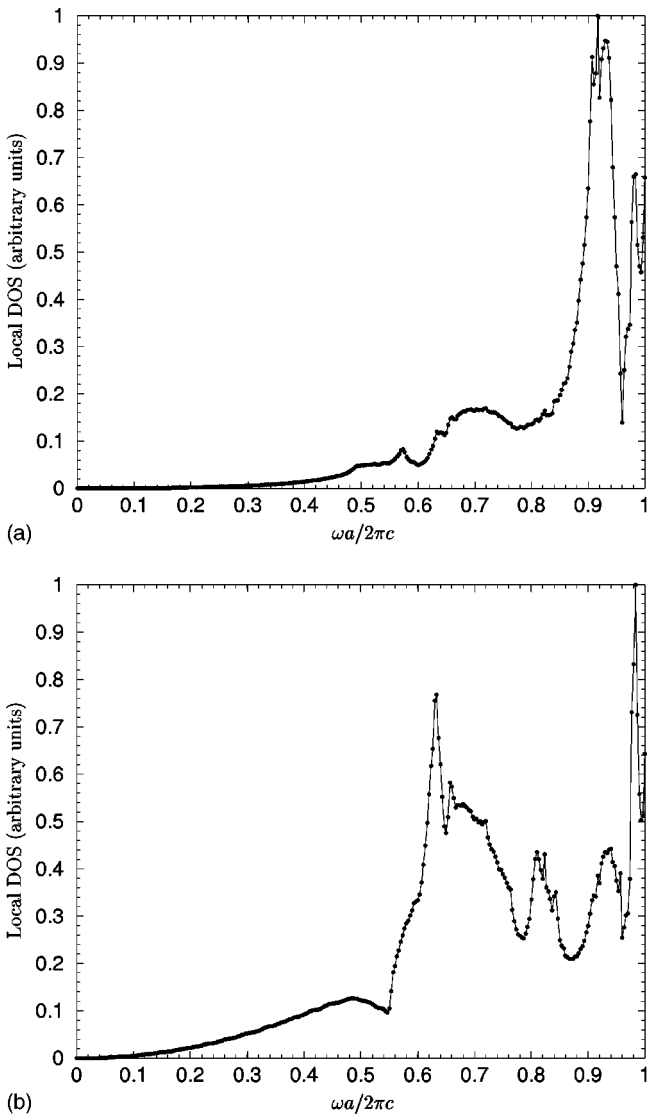

FIG. 2. Local DOS at the center of TiO_2 spheres (a) and midway between two adjacent TiO_2 spheres (b) for a fcc lattice of TiO_2 spheres ($\epsilon \approx 7.35$) in water ($\epsilon \approx 1.77$). The filling ratio for TiO_2 is 25%.

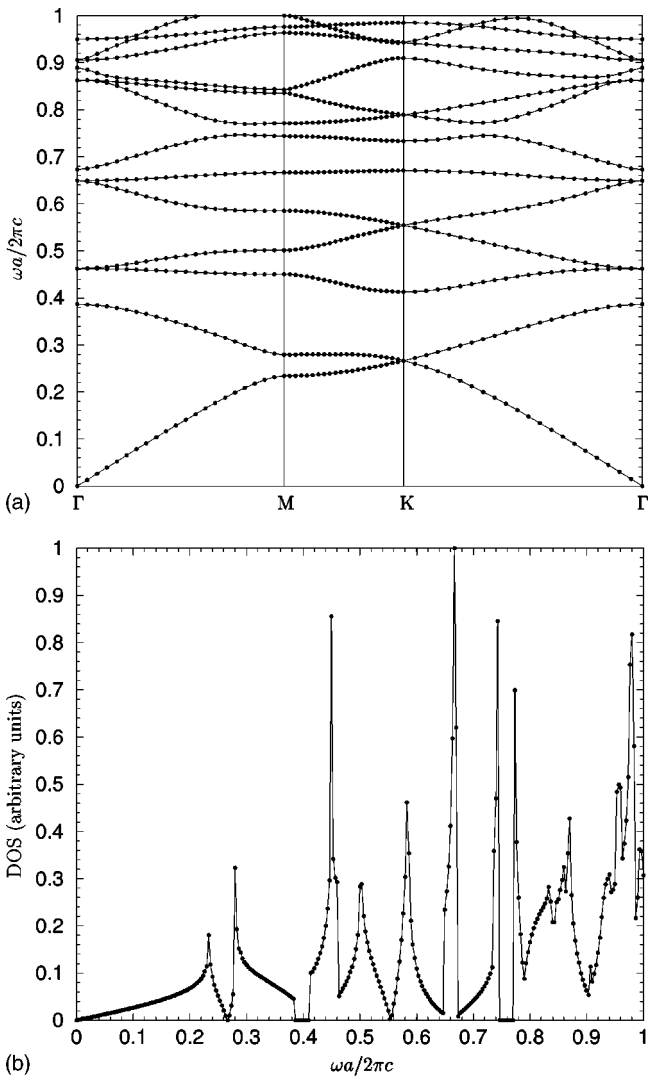

FIG. 3. Two-dimensional band structure (a) (E polarization) and corresponding two-dimensional DOS (b) for a triangular lattice of air cylinders etched into macroporous silicon ($\epsilon \approx 11.9$). The filling ratio for air is 67%.

factors of 2.24 and 2.75, respectively. Further insight is provided through Fig. 2(a). There we show the LDOS for this photonic crystal projected onto the center of a TiO_2 sphere. Clearly, the flank at $\tilde{\omega} = 0.62$ is reduced, whereas the flank around $\tilde{\omega} = 0.9$ is drastically increased to about 4:1. Similarly, Fig. 2(b) shows the LDOS projected onto a point midway between two TiO_2 spheres. We observe that for this location, the flank at $\tilde{\omega} = 0.62$ is enhanced to about 5:1, whereas the flank around $\tilde{\omega} = 0.9$ is strongly reduced.

B. Two-dimensional structures

Another class of photonic crystals with incomplete three-dimensional PBGs are periodic arrays of infinitely extended cylinders, the so-called two-dimensional PBG materials. In particular, for propagation directions perpendicular to the cylinder axis, triangular lattices of air voids in macroporous silicon were shown to possess overlapping two-dimensional PBGs for the two possible transverse polarizations [40,41]. This is illustrated in Figs. 3(a) and 3(b) and Figs. 4(a) and 4(b), where we display the two-dimensional band structure and DOS for E and H polarization, respectively. The structure consists of a triangular array of air cylinders in macroporous silicon ($\epsilon_b \approx 11.9$) with a filling ratio of 33% silicon [41]. The sharp peaks in the DOS are a manifestation of Van Hove singularities characteristic of two-dimensional lattices. Such two-dimensional band gaps may provide the testing ground for a variety of nonlinear optical soliton phenomena predicted in Refs [26–28].

However, for inhibition of spontaneous emission in quantum optical phenomena, the full three-dimensional DOS has to be considered. The corresponding three-dimensional dispersion relation must be computed by solving the full vector problem Eq. (10) rather than Eq. (4) or (7). Similarly, the integration in three-dimensional k space, Eq. (17) or (18), has to be performed with an appropriate cutoff in the k_z direction. In the present case of a triangular lattice the k-space integration domain is a hexagonal prism and the cutoff is determined by $k_z^{\max} = (\omega/c)\max(\sqrt{\epsilon_a}, \sqrt{\epsilon_b})$. Figure 5 dis-

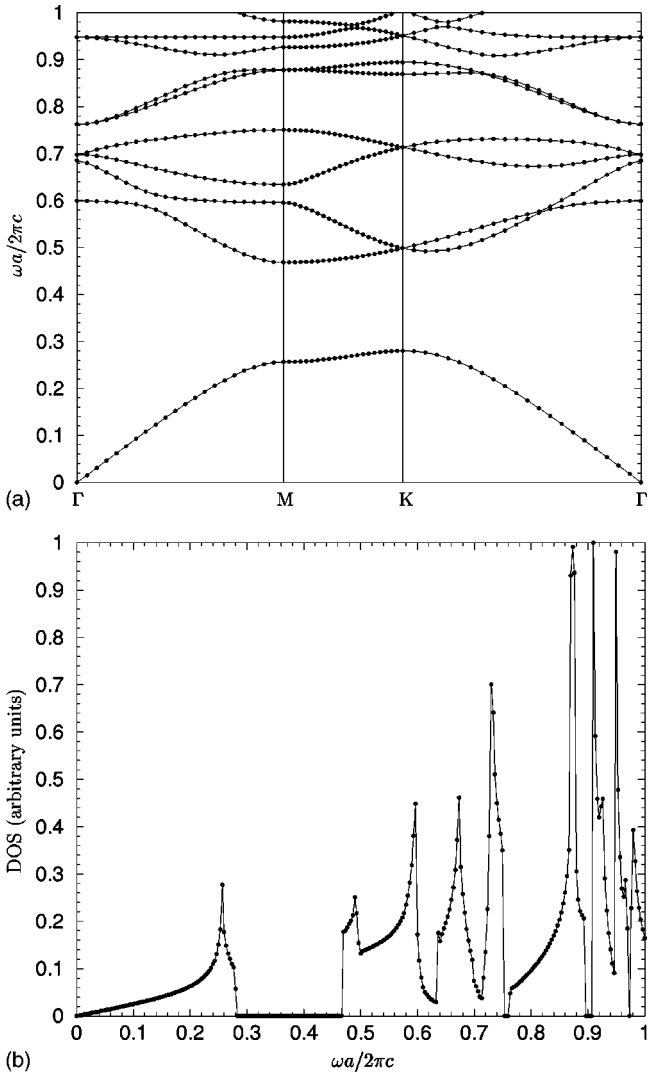

FIG. 4. Two-dimensional band structure (a) (H polarization) and corresponding two-dimensional DOS (b) for a triangular lattice of air cylinders etched into macroporous silicon ($\epsilon \approx 11.9$). The filling ratio for air is 67%.

plays the total three-dimensional DOS for the same structure as in Figs. 3 and 4. Clearly, there is no complete three-dimensional PBG for such a structure. The two-dimensional gaps now manifest themselves in fluctuations of the three-dimensional DOS. In particular, the gaps of the E polarization appear to have a more profound effect on the three-dimensional DOS than do the gaps of the H polarization. However, the overall fluctuations of the three-dimensional DOS are weaker than in the case of the fcc lattice of TiO_2 spheres in water.

For the structure considered above we find a sharp variation in the total DOS around $\tilde{\omega} \approx 0.43$ with magnitude 2:1. At locations midway between adjacent cylinders this variation is reduced [Fig. 6(a)], whereas it is shifted to $\tilde{\omega} \approx 0.46$ and enhanced to about 3:1 at the center of the cylinders [Fig. 6(b)].

IV. INVERTED OPALS

The results of the preceding section demonstrate the necessity of a three-dimensional photonic crystal with the appropriate network topology for creation of a complete PBG in three dimensions. The diamond or diamondlike structures known to possess complete gaps are very expensive to microfabricate by either reactive ion etching or layer by layer growth on the length scales required for PBGs in the visible. Moreover, these techniques lead to relatively small samples of length less than ten lattice constants. Self-assembling structures hold the promise of very large size samples with PBGs in the visible. Binary colloids are discussed at length in Ref. [49], but may be very difficult to realize. Here we concentrate on photonic crystals based on inverted opals. These are manufactured by using either emulsion templating [50] or infiltration of artificial opals with high dielectric material [51]. As we demonstrate below, the quality of currently available artificial opals [46–48] makes their controlled infiltration a goal worth striving for.

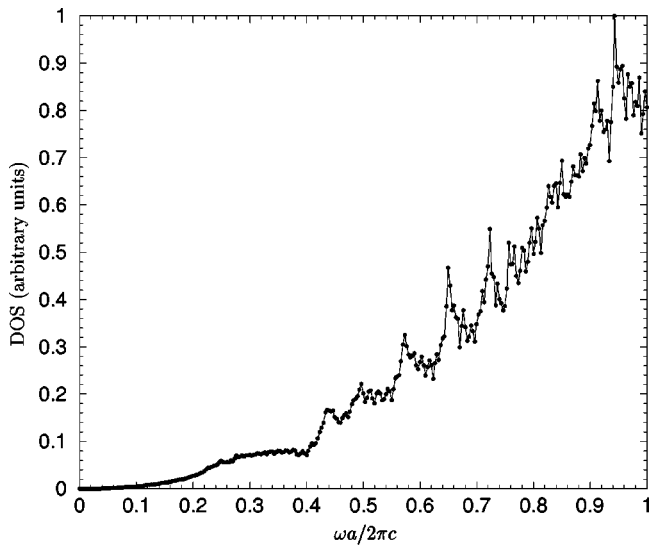

FIG. 5. Three-dimensional total DOS for a triangular lattice of air cylinders etched into silicon ($\epsilon \approx 11.9$). The filling ratio for air is 67%.

A. Artificial opals

Artificial opals themselves come as close-packed structures of monodisperse SiO_2 spheres with dielectric constants ranging from $\epsilon_a = 2.1$ for bulk SiO_2 down to $\epsilon_a = 1.59$ for spheres of diameter 0.2 μm. Similar to the case of TiO_2 spheres in water, no complete gap is found for any filling ratio f of the SiO_2 spheres. A typical total DOS is shown in Fig. 7.

However, it has long been known that the inverted fcc structure, i.e., close-packed low dielectric spheres in a high dielectric matrix possess a complete PBG [59]. We present below a detailed study of inverted structures that are currently being manufactured [51].

B. Infiltration of opals with various dielectrics

The recipe of producing inverted structures from artificial opals is to infiltrate them with a high dielectric material and to subsequently etch out the SiO_2 spheres, leaving behind a connected network of high dielectric material with filling ratios around $f = 0.26$ (''Swiss cheese structures''). The etch-

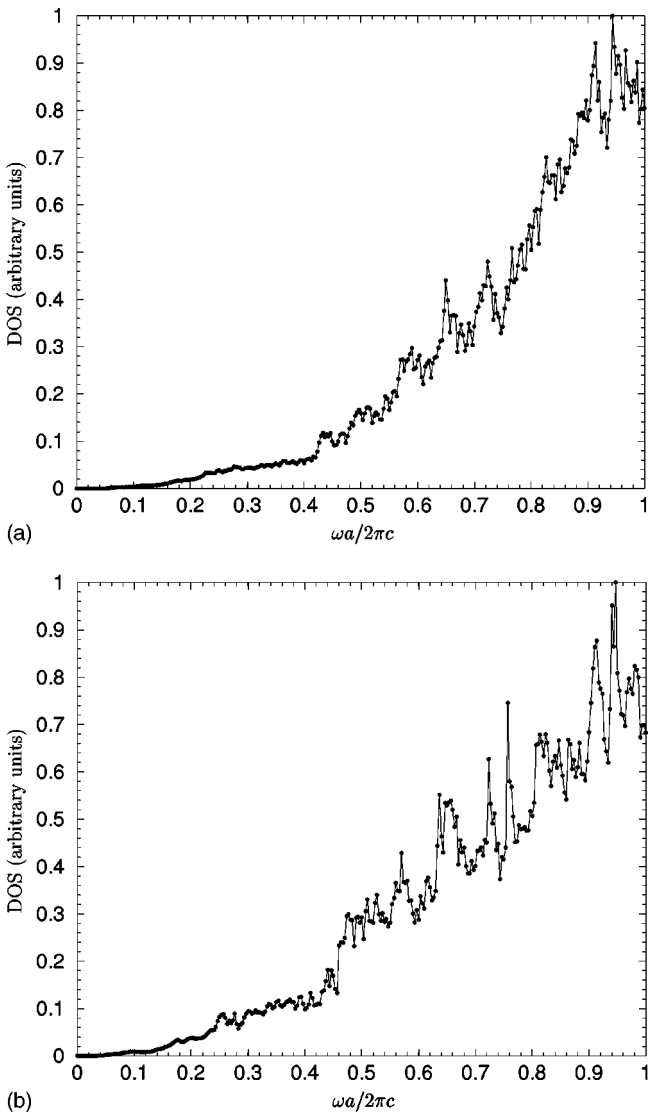

FIG. 6. Three-dimensional LDOS midway between two adjacent cylinders (a) and at the center of the cylinders (b) for a triangular lattice of air cylinders etched into silicon ($\epsilon \approx 11.9$). The filling ratio for air is 67%.

ing out of the SiO_2 enhances the dielectric contrast, which in turn leads to larger gaps. Moreover, the presence of air voids rather than solid SiO_2 will greatly ease the injection of atomic vapors with which quantum optical experiments can be carried out and also facilitates the infiltration by active materials such as conducting polymers and dyes for laser applications. In Figs. 8(a) and 8(b) as well as Figs. 9(a) and 9(b) we present the band structure and corresponding total DOS of an inverted fcc and hcp structure consisting of close-packed air spheres in a silicon matrix with dielectric constant $\epsilon_b \approx 11.9$. We observe that the fcc structure possesses a pseudogap between the fourth and fifth bands around $\tilde{\omega} \approx 0.524$ and a complete 4.25% band gap between the eighth and ninth bands with a center frequency of $\tilde{\omega} \approx 0.794$. Similarly, the hcp structure exhibits a less pronounced pseudogap between the eighth and ninth bands around $\tilde{\omega} \approx 0.364$ and a complete 2.8% gap between the 16th and 17th bands with a

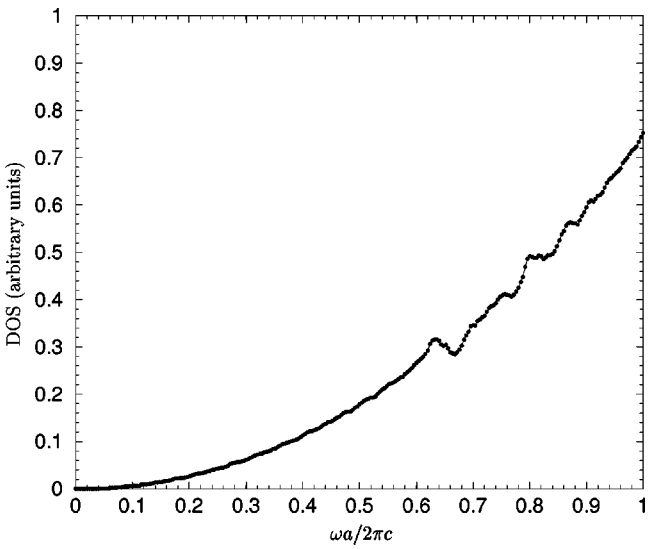

FIG. 7. DOS for a close-packed fcc lattice of silica spheres ($\epsilon \approx 2.1$) in air (opal).

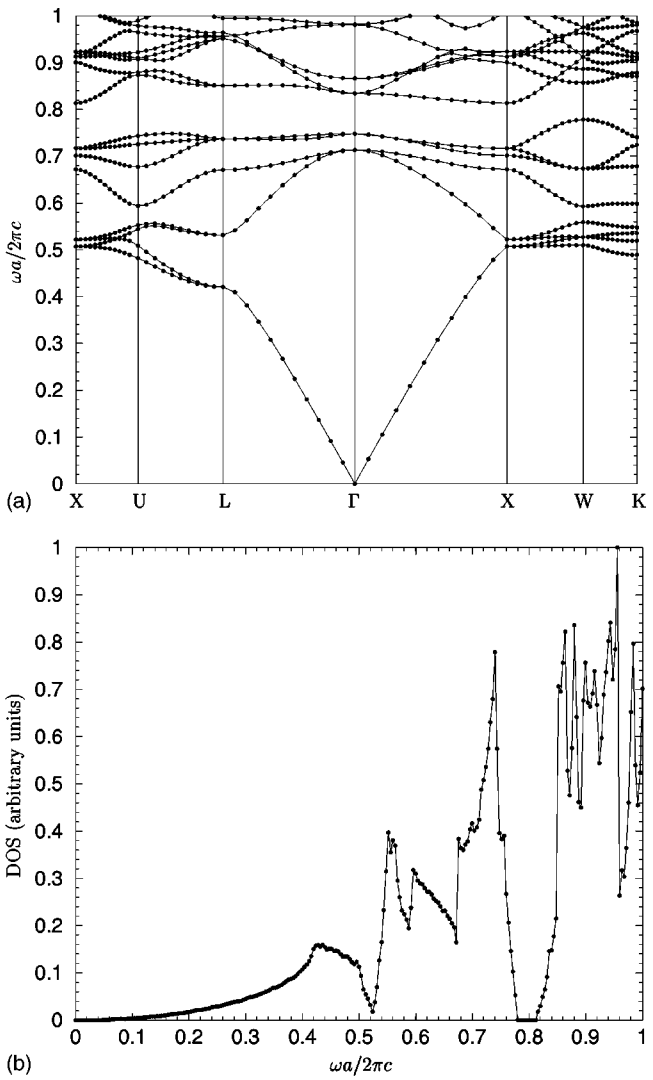

FIG. 8. (a) Band structure (a) and corresponding DOS (b) for a close-packed fcc lattice of air spheres in silicon ($\epsilon \approx 11.9$).

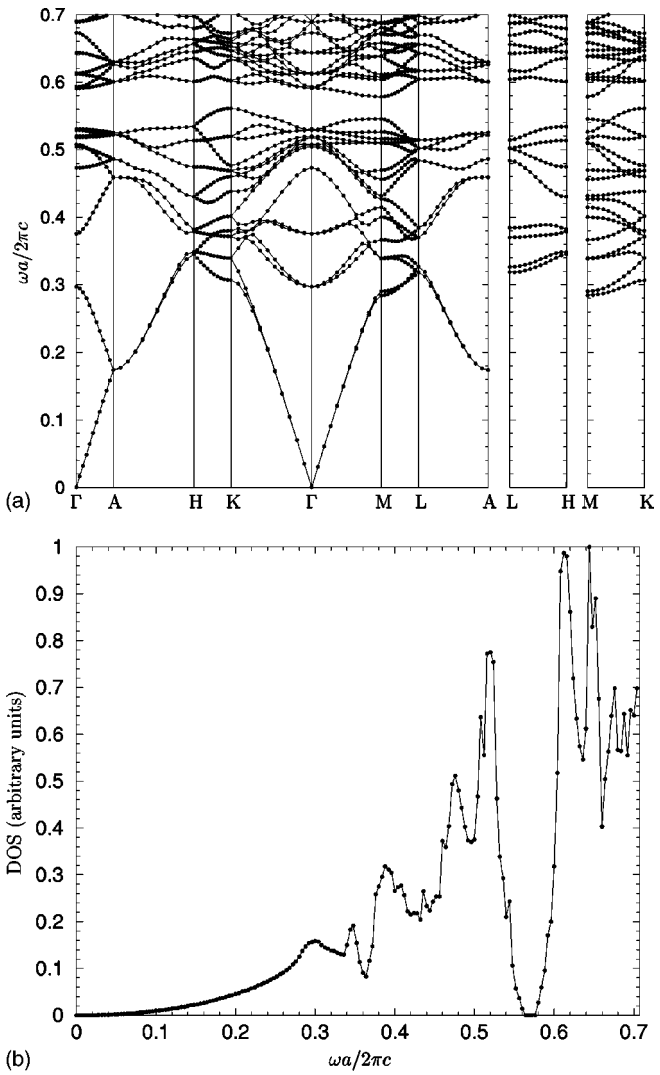

FIG. 9. Band structure (a) and corresponding DOS (b) for a close-packed hcp lattice of air spheres in silicon ($\epsilon \approx 11.9$). Note that the lattice constant of a close-packed hcp lattice is, by a factor of $\sqrt{2}$, smaller than the lattice constant of the corresponding close-packed fcc lattice.

center frequency $\tilde{\omega} \approx 0.570$. The occurrence of the pseudogap as well as the complete gap between higher bands for the hcp structure stems from the fact that the hcp crystal constitutes a hexagonal lattice with a two atom basis. In addition, the lattice constants of fcc and hcp structure differ by a factor of $\sqrt{2}$, so that the pseudogap and complete gap occur at roughly the same frequencies for both structures.

Figure 10 shows the dependence of the gap size of the inverted close-packed fcc lattice as a function of the background index of refraction. Materials such as silicon ($n \approx 3.45$) and germanium ($n \approx 4.0$) produce band gaps of a relative size $\Delta\omega/\omega_0 \approx 4.25\%$ and $\Delta\omega/\omega_0 \approx 7.35\%$, respectively. Figure 11 displays the dependence of the relative gap size for the inverted silicon fcc structure on the radius of the air spheres. Obviously, there exists an optimal filling ratio for slightly overlapping spheres that maximizes the gap. While the difference from the close-packed structure is small, this raises the interesting question whether a more clever approach for removing material from the close-packed structure would lead to a larger band gap.

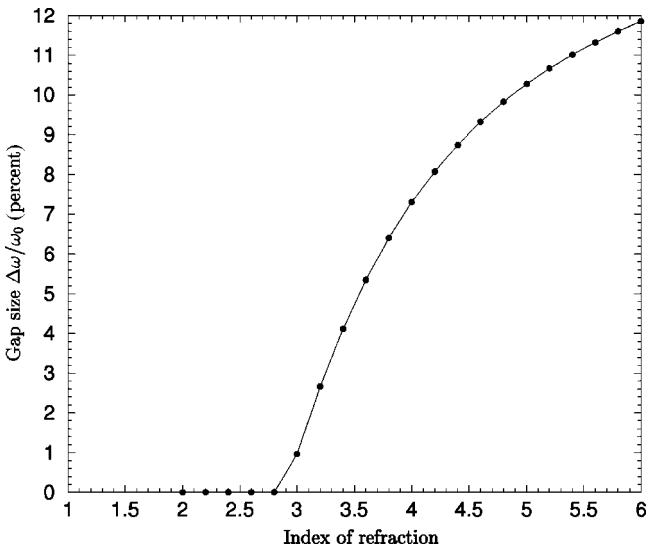

FIG. 10. Dependence of the gap size as a function of index of refraction for a close-packed fcc lattice of air spheres in a high dielectric matrix.

C. Effect of sintering and incomplete infiltration

The manufacturing process of infiltrated opals itself suggests two possible approaches to enlarging the PBG. (i) Sintering the artificial opal prior to infiltration, improves the stability of the structure and makes it easier to handle. With sintering, the formerly touching spheres are now bonded by a tubelike connection. Infiltrating this sintered structure will result in an inverted structure with a slightly smaller filling ratio of high dielectric material. (ii) In practice, the infiltration of a close-packed opal structure may lead only to an incomplete occupation of the void regions between the SiO_2 spheres. This can be modeled by assuming that the high index material (Si or Ge) ''wets'' the surface of the SiO_2 spheres up to a certain thickness. After removal of the SiO_2 the resulting structure consists of air spheres coated with

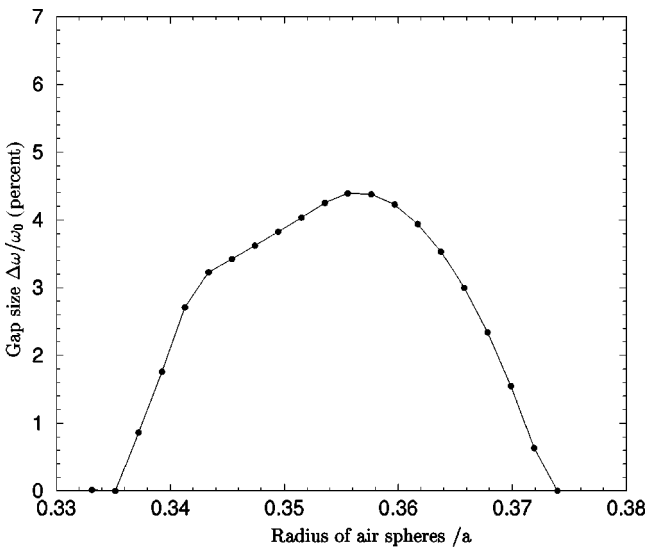

FIG. 11. Dependence of the gap size as a function of radius for a fcc lattice of air spheres in silicon ($\epsilon \approx 11.9$) near close packing. The sphere radius is measured in units of the cubic lattice constant a. $r = a/\sqrt{8} \approx 0.3536a$ corresponds to exact close packing.

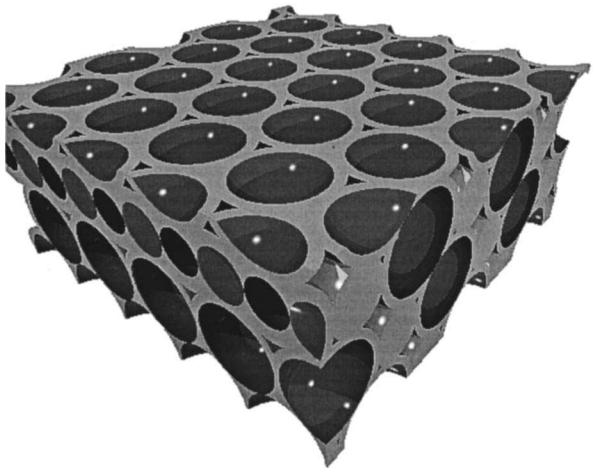

FIG. 12. Cross-sectional view through an incompletely infiltrated opal. After etching out the SiO_2 spheres, the incomplete infiltration of silicon (gray) results in additional air voids between hollow spheres, which appear as triangular or diamond shaped holes on the surface of the cut.

high dielectric material rather than consisting of air spheres in an entirely filled high dielectric matrix. This structure with a small interstitial void between air spheres is depicted in Fig. 12.

Figure 13 shows the dependence of the relative gap size of the inverted fcc structure on sintering the artificial opal prior to infiltration. Here we assume that sintering the artificial opal leads to the formation of tubes connecting the sphere centers of adjacent touching spheres. Accordingly, we plot in Fig. 13 the gap size of silicon-infiltrated artificial opals on the radius R_s of the sintering tube. Clearly, there is a drastic enhancement of the gap size for a tube radius around $R_s \approx 0.133a$, where a is the lattice constant of the fcc lattice. This result is consistent with similar results obtained by Chan *et al.* [14] for the $A7$ structure. Both cases support the concept that PBG formation is enhanced by the presence

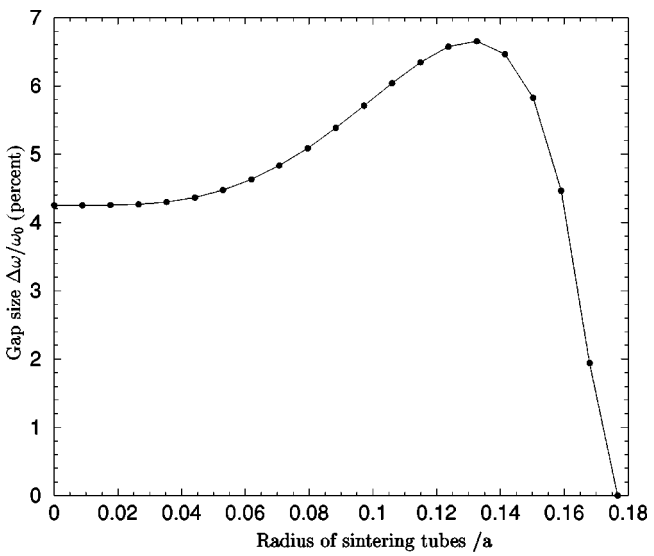

FIG. 13. Dependence of the gap size as a function of radius of sintering tubes for a close-packed fcc lattice of air spheres in silicon ($\epsilon \approx 11.9$). The tube radius is measured in units of the cubic lattice constant a.

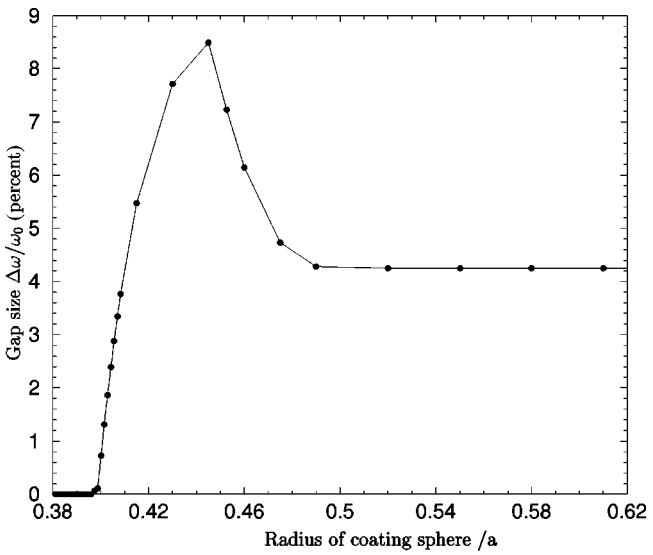

FIG. 14. Dependence of the gap size as a function of radius of coating for a close-packed fcc lattice of air spheres coated with silicon ($\epsilon \approx 11.9$). The coating radius is measured in units of the cubic lattice constant a.

of a true network topology since sintering improves the connectivity of the air fraction. Once the sintering radius exceeds a certain value, infiltrating the sintered opal does not deposit enough high dielectric material to sustain the band gap and it quickly collapses.

Figure 14 displays the dependence of the gap size of the inverted fcc structure on the degree of incomplete infiltration. Again, we choose to plot the results of the silicon-infiltrated artificial opal, where silicon is now assumed to form a coating of the closed-packed air spheres. We observe that a slightly incomplete infiltration actually leads to a strong enhancement of the gap size compared to the completely infiltrated structure. For a coating radius of $R_c \approx 0.445a$ (corresponding to about 21% total volume fraction of silicon) the gap size of the incompletely infiltrated structure is doubled compared to the fully infiltrated one. Once again, as the infiltration becomes more and more incomplete, the band gap eventually disappears altogether as there is not enough high dielectric material to sustain a band gap.

We have performed similar studies on the hcp structure and found analogous dependences of the gap size on the background dielectric constant, sphere radius, radius of sintering tubes, and coating radius for incomplete infiltration. Overall, the gap size for a given inverted hcp structure is generally a little smaller than the gap size of the corresponding inverted fcc structure.

D. Tuning the PBG through the application of strain

Another line of thought concerns the mechanical manipulation of the artificial opal prior to its infiltration with high dielectric material. Exerting not too large pressure on the opal will result in slight deviations from the fcc or hcp close-packed structures. The effect may be twofold. First, the position and size of the complete gaps may be changed, thereby allowing one to tune the PBG material. Second, applying strain reduces the symmetry of the photonic crystal relative to that of the unstrained PBG material. This lifts certain de-

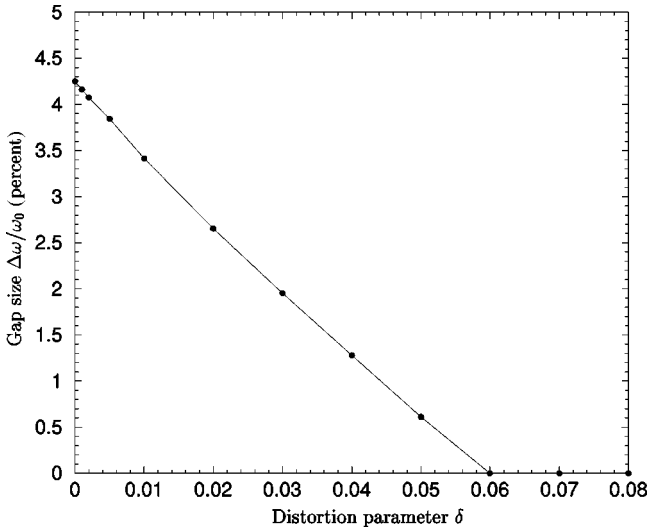

FIG. 15. Dependence of the gap size as a function of the deviation of the z axis from the cubic axis for a close-packed fcc lattice of air spheres in silicon ($\epsilon \approx 11.9$). The structure is pressured along the z axis. See the text for details on the distortion parameter δ.

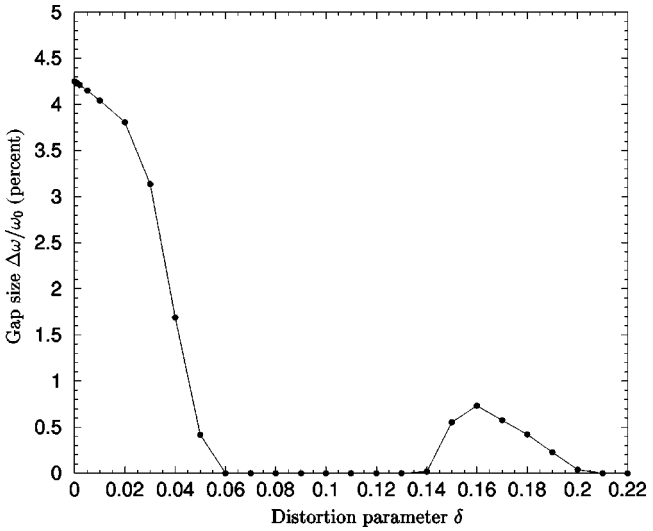

FIG. 16. Dependence of the gap size as a function of the deviation of the body diagonal from ideally cubic for a close-packed fcc lattice of air spheres in silicon ($\epsilon \approx 11.9$). The structure is pressured along the cubic body diagonal. See the text for details on the distortion parameter δ.

generacies of the lattice structure and holds out the possibility of opening the pseudogaps of these structures into complete PBGs.

1. Pressure along the cubic axis on a fcc structure

As a first example, we consider applying pressure along a cubic axis of the fcc lattice of close-packed spheres. This leads to a deformation of the crystal structure in which there is a reduction of the lattice constant for this particular direction. By virtue of the incompressibility of the spheres themselves, this also leads to an increase in the lattice constant perpendicular to the axis of applied pressure. Taking the axis of applied force to be the z axis, the original fcc structure changes to a face centered tetragonal lattice, which is described by the primitive lattice vectors

$$\vec{a}_1 = \frac{a'}{2}(1,1,0), \tag{20}$$

$$\vec{a}_2 = \frac{a'}{2}(1,0,c/a'), \tag{21}$$

$$\vec{a}_3 = \frac{a'}{2}(0,1,c/a'). \tag{22}$$

The parameters c and a' are defined through a strain parameter δ, which measures the deviation of the strained lattice from the unstrained fcc lattice. In particular, $c = a(1-\delta)$ is the side length of the distorted cube along the direction of compression and $a' = a\sqrt{1+2\delta-\delta^2}$ is the increased lattice constant perpendicular to the compression axis. In Fig. 15 we show the dependence of the gap size on the distortion parameter δ of an inverted structure of touching air spheres in silicon ($\epsilon \approx 11.9$), starting from the unstrained inverted close-packed fcc lattice ($\delta = 0$). As a consequence of pressure, the band gap reduces in size and ultimately disappears for $\delta \approx 0.06$. The reduction in symmetry from cubic to tetragonal, however, is not sufficient to convert the pseudogap between bands 4 and 5 of the fcc structure into a full band gap.

2. Pressure along the body diagonal of a fcc structure

An alternative way of straining the fcc crystal is to exert pressure along the cubic body diagonal. This changes the fcc symmetry to a rhombehedrical one ($A7$ symmetry) and is expressed by the set of primitive lattice vectors

$$\vec{a}_1 = \frac{a'}{2}(1,1,\delta), \tag{23}$$

$$\vec{a}_2 = \frac{a'}{2}(1,\delta,1), \tag{24}$$

$$\vec{a}_3 = \frac{a'}{2}(\delta,1,1), \tag{25}$$

where $a' = a/\sqrt{1+\delta^2/2}$ and δ parametrizes the resulting deformation. This deformation may conveniently be described by the angle α between any two primitive lattice vectors, which in the case of an unstrained fcc structure is 60°. In terms of the parameter δ we have $\cos\alpha = (1-2\delta)/(2+\delta^2)$. In Fig. 16 we display the dependence of the relative gap size on the distortion parameter δ. As in the case of pressure along the cubic axis, we observe a closing of the gap as the pressure is increased. Increasing the pressure beyond a certain value, however, reopens the gap again, albeit with a smaller size. For even higher pressure the gap closes again. In order to make sure that this reopening of the band gap is not an artifact of the numerics, we increased the number of reciprocal lattice vectors to 1200 and did not find any changes in the gap size or the band structure. For larger dielectric contrast, the maximum size of the reopened gap increases. As in the case of pressure along the cubic axis, we find that pressure along the cubic body diagonal facilitates tunability of

the higher PBG but fails to convert the lower-frequency pseudogap into a complete gap.

V. DISCUSSION

In summary, we have evaluated the photonic band structures of various self-assembling photonic crystals from the standpoint of optimizing and tuning the resulting PBG in the microfabrication process. A comparison between total DOS and LDOS for structures with incomplete band gaps suggests that certain quantum optical phenomena that rely on rapid variations of the LDOS may occur even in materials that do not exhibit a complete PBG. The LDOS shows considerable variations within a Wigner-Seitz cell. For special locations within the Wigner-Seitz cell certain variations of the total DOS may be suppressed and others may be more pronounced. These results may provide a useful guide for doping the photonic crystal with active molecules and subsequent quantum optical experiments. Our detailed study of inverted opals suggests that both close-packed fcc and hcp structures exhibit full band gaps at roughly the same frequency provided the infiltrating material provides a refractive index contrast of 2.8 or greater. The hcp gap is somewhat smaller than the fcc gap. In addition, we found that the size of the gap can be substantially altered by various procedures. In particular, sintering the opals prior to infiltration may lead to an 80% enhancement of the gap size. Similarly, incomplete infiltration may effectively double the gap size. Distortions of the inverted fcc structure generally seem to reduce the gap size. However, for increasing pressure along the cubic body diagonal we found that the gap may open again.

ACKNOWLEDGMENTS

We are grateful to Dr. Willem Vos, Dr. Ray Baughman, and Dr. Anvar Zakhidov for some helpful discussions. K. B. would like to acknowledge the financial support by the Deutsche Forschungsgemeinschaft (DFG) under Grant Bu 1107/1-1. This work was supported in part by the New Energy and Industrial Technology Development Organization of Japan and by Photonics Research Ontario.

APPENDIX: EVALUATION OF BRILLOUIN ZONE INTEGRALS

In this Appendix we discuss the evaluation of Brillouin zone integrals of the form

$$\int_{1.\mathrm{BZ}} d^d k \; f(\vec{k})\,\delta(\omega-\omega(\vec{k})), \tag{A1}$$

where d denotes the dimensionality. Such integrals are relevant to the total DOS [Eq. (17)], for which $f(\vec{k})\equiv 1$, and the projected (local) DOS [Eq. (18)], for which $f(\vec{k}) \equiv |\vec{E}_{\vec{k}}(\vec{r})|^2$. We evaluate such integrals using the linear tetrahedron method [55] in its symmetry corrected form [56]. For brevity we restrict ourselves to the case of two-dimensional Brillouin zones and refer the reader to electronic band structure literature [55,56] for the analogous three-dimensional calculations.

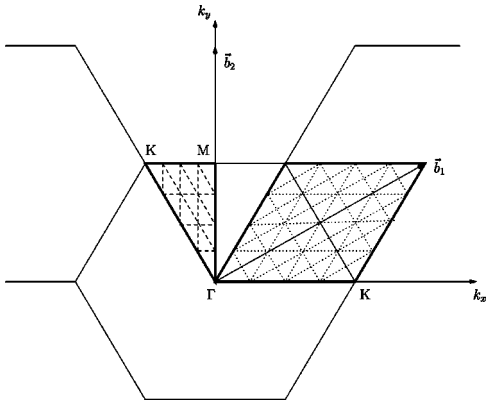

FIG. 17. Region of two-dimensional k space around the first BZ of a triangular lattice. The triangle enclosed by bold lines shows a possible naive discretization of the irreducible part of the BZ, illustrating a misweighting of k points. For instance, in this discretization M, K, and Γ all receive the same weight, which is not compatible with their symmetry-induced multiplicity. In contrast, the discretization of the rhombus enclosed by bold lines generates weights for the various k points that are in accordance with their symmetry-induced multiplicity.

1. Symmetry-corrected discretization

In the linear tetrahedron method [55], the integral over the first Brillouin zone, Eq. (A1), is replaced by a sum of integrals over nonoverlapping triangles (tetrahedra in three dimensions) filling the irreducible part of the first Brillouin zone. The vertices of the triangles (tetrahedra) define a mesh of points in k space $\{\vec{k}_i, i=1,...,N\}$. For each k point $\vec{k}_i$, $f(\vec{k}_i)$ as well as $\omega(\vec{k}_i)$ can be evaluated using the methods outlined in Sec. II. Inside the triangles, the integration is carried out analytically by using linear interpolation between the vertices. However, as pointed out by Kleinman [60], the original linear tetrahedron method of Ref. [55] introduces a relative weight for each k point that is not consistent with its symmetry induced multiplicity. As a consequence, this misweighting produces an unexpectedly large error for the number of k points commonly used in realistic calculations [60]. In addition, quantities calculated in this manner do not satisfy crystal symmetry. This situation is illustrated in Fig. 17, where we display a region of k space around the first BZ of a triangular lattice. The standard discretization of the linear tetrahedron method is illustrated in the left part of the figure. In particular, using this method, the high symmetry points Γ, M, and K are assigned relative weights of 1, 1, and 1, respectively, whereas their symmetry-induced multiplicities are 1, 2, and 3, respectively.

A way to overcome this shortcoming of the linear tetrahedron method was pointed out by Kleinman [60] and was later refined by Hama *et al.* [56]. We illustrate the basic principle in the right part of Fig. 17. There we have artificially enlarged the domain of integration to a rectangle of four times the size of the irreducible part of the first BZ. Clearly, the values of $f(\vec{k})$ and $\omega(\vec{k})$ for the k points of the newly added triangles can, by symmetry, be obtained from corresponding values in the irreducible part of the first BZ.

It is easily checked that the linear tetrahedron method applied to this enlarged integration domain induces a weighting of the k points that is compatible with their symmetry-

induced multiplicity. Similar enlargements of the integration domain without having to evaluate $f(\vec{k})$ and $\omega(\vec{k})$ at more k points can be derived for the square and three-dimensional lattices [56]. In computing the total as well as the local DOS, we have made extensive use of this symmetry-corrected version of the linear tetrahedron method.

2. Integration over a single triangle

Once the correct weighting for the mesh of k points has been restored, it is necessary to derive an expression for the integration over a single triangle using the linear tetrahedron method. As mentioned above, both $f(\vec{k})$ and $\omega(\vec{k})$ are linearly interpolated within a triangle:

$$\omega(\vec{k}) = \omega_1 + \vec{a}\cdot(\vec{k}-\vec{k}_1), \tag{A2}$$

where

$$a_1 = \frac{1}{2A_t}(\Delta\omega_{21}\Delta k_{31}^{(2)} - \Delta\omega_{31}\Delta k_{21}^{(2)}), \tag{A3}$$

$$a_2 = \frac{1}{2A_t}(\Delta\omega_{31}\Delta k_{21}^{(1)} - \Delta\omega_{21}\Delta k_{31}^{(1)}), \tag{A4}$$

$$A_t = \frac{1}{2}(\Delta k_{21}^{(1)}\Delta k_{31}^{(2)} - \Delta k_{31}^{(1)}\Delta k_{21}^{(2)}), \tag{A5}$$

with $\omega_i = \omega(\vec{k}_i)$, $\Delta\omega_{ij} = \omega_i - \omega_j$, and $\Delta\vec{k}_{ij} = (\Delta k_{ij}^{(1)}, \Delta k_{ij}^{(2)}) = \vec{k}_i - \vec{k}_j$. The indices $i,j = 1,2,3$ with $i \neq j$ label the vertices of the triangle. Analogous expressions may be derived for $f(\vec{k}) = f_1 + \vec{b}\cdot(\vec{k}-\vec{k}_1)$. Thus the integral over a single triangle is approximated by

$$\int_{\text{triangle}} d^2k\, f(\vec{k})\,\delta(\omega-\omega(\vec{k})) \approx \int_{\omega=\omega(\vec{k})} dS[f_1 + \vec{b}\cdot(\vec{k}-\vec{k}_1)]\frac{1}{|\vec{a}|}. \tag{A6}$$

The evaluation of the remaining integrals is a straightforward task. Assuming that the vertices of the triangle are labeled such that $\omega_1 \leqslant \omega_2 \leqslant \omega_3$, we obtain for the case of $\omega_1 \leqslant \omega \leqslant \omega_2$

$$\begin{aligned}\int_{\text{triangle}} d^2k\, f(\vec{k})\,\delta(\omega-\omega(\vec{k})) &\approx 2A_t(f_1 - \vec{b}\cdot\vec{k}_1)\frac{\omega-\omega_1}{\Delta\omega_{21}\Delta\omega_{31}} \\ &\quad + 2A_t\vec{b}\cdot\left(\vec{k}_1 + \frac{1}{2}(\omega-\omega_1)\sum_{i=2}^{3}\frac{\vec{k}_i-\vec{k}_1}{\Delta\omega_{i1}}\right) \\ &\quad \times\frac{\omega-\omega_1}{\Delta\omega_{21}\Delta\omega_{31}},\end{aligned} \tag{A7}$$

whereas the case of $\omega_2 \leqslant \omega \leqslant \omega_3$ yields

$$\begin{aligned}\int_{\text{triangle}} d^2k\, f(\vec{k})\,\delta(\omega-\omega(\vec{k})) &\approx 2A_t(f_1 - \vec{b}\cdot\vec{k}_1)\frac{\omega_3-\omega}{\Delta\omega_{31}\Delta\omega_{32}} \\ &\quad + 2A_t\vec{b}\cdot\left(\vec{k}_3 + \frac{1}{2}(\omega-\omega_3)\sum_{i=1}^{2}\frac{\vec{k}_i-\vec{k}_3}{\Delta\omega_{i3}}\right) \\ &\quad \times\frac{\omega_3-\omega}{\Delta\omega_{31}\Delta\omega_{32}}.\end{aligned} \tag{A8}$$

The above set of formulas allows a convenient and efficient way to accurately compute integrals of the type of Eq. (A1). Their generalization to the three-dimensional case of integration over a single tetrahedron may be found in Ref. [55].

[1] E. Yablonovitch, Phys. Rev. Lett. **58**, 2059 (1987).
[2] S. John, Phys. Rev. Lett. **58**, 2486 (1987).
[3] J. Opt. Soc. Am. B **10** (2) (1993), special issue on PBG materials, edited by C. M. Bowden, J. P. Dowling, and H. O. Everitt.
[4] *Photonic Band Gaps and Localization,* edited by C.M. Soukoulis (Plenum, New York, 1993).
[5] J. Mod. Opt. **41** (2) (1994), special issue on PBG materials, edited by G. Kurizki and J. W. Haus.
[6] *Photonic Band Gap Materials*, edited by C.M. Soukoulis (Kluwer Academic, Dordrecht, 1996).
[7] S. John, Phys. Rev. Lett. **53**, 2169 (1984).
[8] S. John, Phys. Today **44** (5), 32 (1991).
[9] D. Wiersma, P. Bartelini, A. Lagendijk, and R. Righini, Nature (London) **390**, 671 (1997).
[10] S. John and R. Rangarajan, Phys. Rev. B **38**, 10 101 (1988).
[11] K.-M. Ho, C.T. Chan, and C.M. Soukoulis, Phys. Rev. Lett. **65**, 3152 (1990).
[12] E. Yablonovitch, T. J. Gmitter, and K. M. Leung, Phys. Rev. Lett. **67**, 2295 (1991).
[13] K.-M. Ho, C.T. Chan, C.M. Soukoulis, R. Biswas, and M. Sigalas, Solid State Commun. **89**, 413 (1993).
[14] C.T. Chan, S. Datta, K.-M. Ho, and C.M. Soukoulis, Phys. Rev. B **50**, 1988 (1994).
[15] S. Fan, P.R. Villeneuve, R. D. Meade, and J.D. Joannopoulos, Appl. Phys. Lett. **65**, 1466 (1994).
[16] K.M. Leung, Phys. Rev. B **56**, 3517 (1997).
[17] E. Özbay, A. Abeyta, G. Tuttle, M. Tringides, R. Biswas, C.T. Chan, C.M. Soukoulis, and K.M. Ho, Phys. Rev. B **50**, 1945 (1994).
[18] E. Özbay, E. Michel, G. Tuttle, R. Biswas, M. Sigalas, and K.M. Ho, Appl. Phys. Lett. **64**, 2059 (1994).

[19] E. Özbay, G. Tuttle, J.S. McCalmont, R. Biswas, C.M. Soukoulis, and K.M. Ho, Appl. Phys. Lett. **67**, 1969 (1995).
[20] E.R. Brown, C.D. Parker, and O.B. McMahon, Appl. Phys. Lett. **64**, 3345 (1994).
[21] S.D. Cheung, R. Biswas, E. Özbay, J.S. McCalmont, G. Tuttle, and K.M. Ho, Appl. Phys. Lett. **67**, 3399 (1995).
[22] M. Sigalas, J.S. McCalmont, K.M. Ho, and G. Tuttle, Appl. Phys. Lett. **68**, 3525 (1996).
[23] A. Mekis, J.C. Chen, I. Kurland, S. Fan, P. Villeneuve, and J.D. Joannopoulos, Phys. Rev. Lett. **77**, 3787 (1996).
[24] S.-Y. Lin, V.M. Hietala, S.K. Lyo, and A. Zaslavsky, Appl. Phys. Lett. **68**, 3233 (1996).
[25] K. Sakoda, T. Ueta, and K. Ohtaka, Phys. Rev. B **56**, 14 905 (1997).
[26] S. John and N. Aközbek, Phys. Rev. Lett. **71**, 1168 (1993).
[27] N. Aközbek and S. John, Phys. Rev. E **57**, 2287 (1998).
[28] N. Aközbek and S. John, Phys. Rev. E **58**, 3876 (1998).
[29] S. John and J. Wang, Phys. Rev. Lett. **64**, 2418 (1990).
[30] S. John and J. Wang, Phys. Rev. B **43**, 12 772 (1991).
[31] S. John and T. Quang, Phys. Rev. A **50**, 1764 (1994).
[32] S. Bay, P. Lambropoulos, and K. Molmer, Opt. Commun. **132**, 257 (1996).
[33] S. John and T. Quang, Phys. Rev. Lett. **74**, 3419 (1995).
[34] T. Quang and S. John, Phys. Rev. A **56**, 4273 (1997).
[35] S. John and T. Quang, Phys. Rev. Lett. **78**, 1888 (1997).
[36] S. John and T. Quang, Phys. Rev. Lett. **76**, 2484 (1996).
[37] S. John and V.I. Rupasov, Phys. Rev. Lett. **79**, 821 (1997).
[38] S.L. McCall *et al.*, Phys. Rev. Lett. **67**, 2017 (1991).
[39] W.M. Robertson *et al.*, Phys. Rev. Lett. **68**, 2023 (1992).
[40] U. Grüning, V. Lehmann, and C.M. Engelhardt, Appl. Phys. Lett. **66**, 3254 (1995).
[41] U. Grüning, V. Lehman, S. Ottow, and K. Busch, Appl. Phys. Lett. **68**, 747 (1996).
[42] A. Birner, F. Müller, and U. Gösele (private communication).
[43] I.I. Tarhan and G.H. Watson, Phys. Rev. Lett. **76**, 315 (1996).
[44] R.D. Pradhan, J.A. Bloodgood, and G.H. Watson, Phys. Rev. B **55**, 9503 (1997).
[45] W.L. Vos, R. Sprik, A. van Blaaaderen, A. Imhof, A. Lagendijk, and G.H. Weydam, Phys. Rev. B **53**, 16 231 (1996).
[46] Yu.A. Vlasov, V.N. Astratov, O.Z. Karimov, A.A. Kaplyanskii, V.N. Bogomolov, and A.V. Prokofiev, Phys. Rev. B **55**, R13 357 (1997).
[47] V.N. Bogomolov, S.V. Gaponenko, I.N. Germanenko, A.M. Kapitonov, E.P. Petrov, N.V. Gaponenko, A.V. Prokofiev, A.N. Ponyavina, N.I. Silvanovitch, and S.M. Samoilovitch, Phys. Rev. E **55**, 7619 (1997).
[48] H. Miguez, C. Lopez, F. Meseguer, A. Blanco, L. Vazquez, R. Mayoral, M. Ocana, V. Fornes, and A. Mifsud, Appl. Phys. Lett. **71**, 1148 (1997).
[49] R. Biswas, M.M. Sigalas, G. Subramania, and K.-M. Ho, Phys. Rev. B **57**, 3701 (1998).
[50] A. Imhof and D.J. Pine, Nature (London) **389**, 948 (1997).
[51] R. Baughman and A. Zakhidov (unpublished).
[52] N. W. Ashcroft and N. D. Mermin, *Solid State Physics* (Saunders College, Philadelphia, 1976).
[53] R.D. Meade, A.M. Rappe, K.D. Brommer, J.D. Joannopoulos, and O.L. Alerhand, Phys. Rev. B **48**, 8434 (1993).
[54] P. R. Villeneuve and M. Piche, Prog. Quantum Electron. **18,** 153 (1994).
[55] G. Lehmann and M. Taut, Phys. Status Solidi B **54**, 469 (1972).
[56] J. Hanna, M. Watanabe, and T. Kato, J. Phys. Condens. Matter **2**, 7445 (1990).
[57] B.A. van Tiggelen and E. Kogan, Phys. Rev. A **49**, 708 (1994).
[58] R. Sprik, B.A. van Tiggelen, and A. Lagendijk, Europhys. Lett. **35**, 265 (1996).
[59] H.S. Sözüer, J.W. Haus, and R. Inguva, Phys. Rev. B **45**, 13 962 (1992).
[60] L. Kleinman, Phys. Rev. B **28**, 1139 (1983).